Transportability of hydrate slurry in the presence of wax

Luiz Henrique Meneghel Lino, Gianluca Lavalle, Eric Serris, Jean-Michel Herri, Ana Cameirao, Nicolas Lesage, Annie Fidel-Dufour

Chemical Engineering Science 317 (2025) 122031

Contents lists available at ScienceDirect

Chemical Engineering Science

journal homepage: www.elsevier.com/locate/ces

Transportability of hydrate slurry in the presence of wax

Luiz Henrique Meneghel Lino [a,*], Gianluca Lavalle [a], Eric Serris [a], Jean Michel Herri [a], Ana Cameirao [a], Nicolas Lesage [b], Annie Fidel Dufour [b]

[a] Mines Saint-Etienne, Saint-Etienne, 42000, France
[b] TotalEnergies, Pau, Cedex 64018, France

ARTICLE INFO

Keywords:
Flow assurance
Hydrate
Wax
Multiphase flow
Plug

ABSTRACT

Flow assurance remains a critical challenge in oil and gas production, with hydrate and wax deposition representing two of the most significant risks to safe and continuous operations. This study investigates the coupled transport of gas hydrates and wax in multiphase systems, with a focus on understanding how dispersed wax particles influence hydrate formation and the risk of pipeline plugging. Experiments were performed in a high-pressure flow loop using a water-in-oil emulsion (10 % water cut), where both flow rate and wax concentration were systematically varied. The results demonstrate that the presence of wax significantly reduces the hydrate volume fraction, thereby mitigating plugging risk. For instance, at a flow rate of 400 L/h, the hydrate fraction decreased from 8.6 % in wax-free oil to 1.8 % with 5 wt% wax. This effect is linked to the increased apparent viscosity caused by wax precipitation, which promotes particle agglomeration and reduces the active surface area for hydrate crystallization. These findings offer new insight into the complex interplay between wax and hydrate in multiphase flow systems and suggest that wax presence, under certain conditions, may play a protective role against hydrate plugging.

1. Introduction

Offshore oil and gas production entails the transport of crude oil, formation water, natural gas, and various impurities (e.g., sand and solid deposits) under high-pressure and low-temperature conditions. Subsea production poses numerous technical challenges, among which flow assurance stands out due to its direct impact on production continuity and surface processing operations. Within the scope of flow assurance, the combined occurrence of gas hydrates and wax deposition remains insufficiently explored in the literature. These phenomena are considered among the most critical issues, as they can significantly increase frictional losses or even lead to complete pipeline blockage (Gao, 2008; Theyab, 2018), potentially resulting in severe economic losses.

Gas hydrates are crystalline compounds formed by hydrogen-bonded water molecules (hosts) encapsulating small gas molecules (guests), such as methane, ethane, and carbon dioxide-typical constituents of natural gas (Sloan and Koh, 2007). These structures form under moderate to high pressure and low temperature, although the specific thermodynamic conditions vary according to system composition (Shahnazar and Hasan, 2014). When favorable, hydrate particles can agglomerate and severely compromise flow assurance by plugging pipelines (Sloan, 2010).

Waxes, in turn, are high-molecular-weight paraffinic hydrocarbons that lose solubility as the temperature decreases, resulting in their successive precipitation from higher to lower molecular weights (Hong et al., 2025). This process increases the apparent viscosity of the oil and may lead to wax deposition on pipeline walls if the temperature is sufficiently low. Over time, such deposits can potentially lead to pipeline blockages (Hong et al., 2025). Within the temperature range relevant to petroleum operations, waxes are predominantly composed of hydrocarbons with more than 20 carbon atoms (Coutinho et al., 2002).

Consequently, under the severe thermodynamic conditions typically encountered in offshore production systems, both hydrate formation and wax precipitation are likely to occur simultaneously within the multiphase flow.

The interaction between hydrates and waxes in multiphase systems has been addressed in recent studies; however, the mechanisms involved remain poorly understood. Experimental investigations (Ma et al., 2017; Song et al., 2021; Chen et al., 2018) and molecular dynamics simulations (Zhang et al., 2019) suggest that wax particles can adsorb at the interface of water droplets. Nevertheless, a comprehensive explanation for this phenomenon is still lacking. The presence of a wax layer at the droplet interface has been shown to increase mass transfer resistance for gas molecules, thereby hindering hydrate formation (Chen et al., 2018;

* Corresponding author.
E-mail addresses: l.meneghel@emse.fr (L.H. Meneghel Lino), gianluca.lavalle@emse.fr (G. Lavalle), serris@emse.fr (E. Serris), herri@emse.fr (J.M. Herri), cameirao@emse.fr (A. Cameirao), nicolas.lesage@totalenergies.com (N. Lesage), annie.fidel-dufour@totalenergies.com (A. Fidel Dufour).

https://doi.org/10.1016/j.ces.2025.122031
Received 17 April 2025; Received in revised form 5 June 2025; Accepted 10 June 2025
Available online 14 June 2025

Zhang et al., 2019; Wang et al., 2020). This wax layer may influence hydrate induction time, growth rate, and final volume fraction. Additionally, it affects hydrate morphology (Liu et al., 2022b; Chen et al., 2018) and agglomeration behavior (Zhou et al., 2022), since interfacial mass transfer plays a crucial role in hydrate development.

Xiao et al. (2023) investigated the formation of CO_2 hydrates in the presence of wax and observed a non-monotonic relationship between wax content and induction time. Specifically, induction time increased at low wax concentrations (0.5 wt%) and decreased at higher concentrations (1.5 and 2.5 wt%), which was attributed to an enhanced probability of heterogeneous nucleation. Liu et al. (2022a), using a high-pressure flow loop, studied hydrate formation in a water-in-oil system with wax and anti-agglomerants and concluded that wax shortened induction time. Conversely, other studies (Chen et al., 2018; Song et al., 2023; Tong et al., 2020; Liu et al., 2019; Shi et al., 2018) reported increased induction times, attributed to the elevated diffusion resistance caused by the wax layer.

Experimental results have further demonstrated that hydrate growth rates and cumulative gas consumption tend to decrease in the presence of wax, as observed in both high-pressure autoclaves (Chen et al., 2018; Song et al., 2020; Jing et al., 2023) and flow loop experiments (Liu et al., 2022a, 2019). Chen et al. (2018) hypothesized that wax adsorption on the hydrate shell reduces its porosity and hydrophilicity, thereby decreasing water permeation and, consequently, hydrate growth rates.

However, some studies conducted in high-pressure autoclaves provide inconclusive results regarding the influence of wax on hydrate growth (Wang et al., 2020; Shi et al., 2018). Wang et al. (2020) proposed that the heat released during hydrate nucleation may disrupt or partially dissolve the wax layer, mitigating its impact on growth. Similarly, Shi et al. (2018) argued that wax effects are more pronounced in the initial stages of hydrate formation.

Regarding the transportability of hydrate slurries in high-pressure flow loops, Liu et al. (2018) observed that the presence of wax increased the risk of system plugging. Shi et al. (2018) noted that wax influences hydrate growth rate and final hydrate fraction, with dependencies on operational parameters such as initial pressure and agitation rate. The hydrate slurry exhibited shear-thinning behavior, with apparent viscosity increasing as wax concentration rose. Liu et al. (2022a) attributed the reduction in induction time in wax-containing systems to enhanced heterogeneous nucleation. Furthermore, they reported lower cumulative gas consumption due to increased mass transfer resistance and agglomeration resulting from wax adsorption at interfaces. The study concluded that, while anti-agglomerants may stabilize hydrate slurries and prevent plugging, such stability is not achievable in the presence of wax, even with higher additive concentrations and lower hydrate fractions. Wax was found to exacerbate plugging risk due to coupled agglomeration and synergistic deposition.

In summary, the complex interactions between hydrates and waxes in multiphase flow remain insufficiently characterized. This work aims to address the following question: under realistic multiphase flow conditions, what is the impact of wax on hydrate formation and on the associated risk of pipeline blockage? To this end, the present study investigates the influence of wax on gas hydrate formation and transportability in a water-in-oil system using a multi-sensor flow loop. In contrast to previous experimental setups (Liu et al., 2018, 2019, 2022a), the flow loop employed herein includes an extended horizontal section, several meters in length, capable of emulating pilot-scale flow conditions. Moreover, it is instrumented with multiple sensors, including acoustic emission probes and a particle vision microscope, to enable comprehensive observation of the coupled phenomena. These include the effect of wax on hydrate formation, transport behavior, flow regime transitions, and plugging tendencies.

2. Materials and methods

Experiments are conducted in the Archimede flow loop, shown in Fig. 1, a high-pressure flow loop located at Mines Saint-Etienne. The system consists of horizontal and vertical sections and has a total length of approximately 56 m. It features a circular cross-section with an internal diameter of 15.7 mm. The Archimede setup has previously been used to characterize hydrate slurries under various conditions (Fidel-Dufour et al., 2006; Leba et al., 2010; Melchuna et al., 2016; Pham et al., 2020; De Almeida et al., 2023).

Temperature is controlled via two thermostatic baths connected with the heat exchangers around the pipeline (orange boxes in Fig. 1). Moreover, the pipeline is insulated to avoid heat exchange with the ambient. The pressurization is made by injecting gas from the gas cylinder into the separator, where liquid and gas come into contact. During the operation, pressure is kept constant by a gas compensation system (indicated as GCS in Fig. 1). As gas is dissolved into the liquid or is consumed to form hydrates, the gas compensation system injects gas into the separator to maintain the pressure constant. Furthermore, a progressive cavity pump sustains flow inside the flow loop while preserving particle integrity.

The flow loop is equipped with a comprehensive set of instruments for real-time monitoring of flow parameters, including temperature, pressure, flow rate, density, acoustic emissions (each probe labeled with a number and a letter, where the letter indicates the frequency class: A = 150 kHz, B = 300 kHz, and C = 350 kHz), and flow visualization. These measurements are taken at various intervals using specialized sensors and imaging systems, as summarized in Table 1.

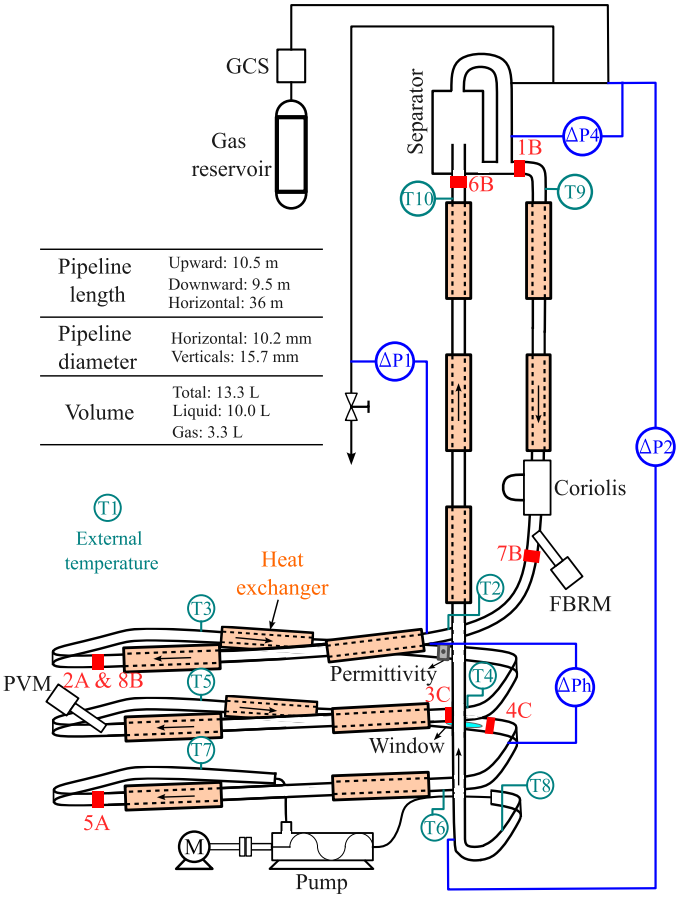

Fig. 1. Schematic representation of the Archimede flow loop.

Table 1
Probes installed on the Archimede flow loop, along with the corresponding notation and feature.

Instrument	Notation	Measurement
Temperature probes	$T_1 - T_{10}$	Flow and external temperature in $^{\circ}C$ every second.
Pressure / Pressure drop probes	P_{abs}, ΔP_1, ΔP_2, ΔP_h, ΔP_4	Absolute pressure and differential pressure probe measured every 1.0 s.
Coriolis	Q, ρ	Mixture flow rate and density.
Gas injection	Q_g, P_g	Gas injection flow rate and absolute pressure.
Acoustic emission	AE	Absolute energy in aJ every 0.5 s from 8 probes.
Focused beam reflectance measurement	FBRM	Chord length and counts every 5 s.
Particle vision microscope	PVM	Images from the flow every 5 s.
Permittivity probe	ε_R	Relative permittivity every 3 to 6 s.
High-speed camera	HSC	Monochromatic images from the flow up to 211 fps.

2.1. Materials

The working materials include synthetic natural gas supplied by Air Products and with its composition listed in Table 2, Kerdane oil, composed by a mixture of $C_{11} - C_{14}$ hydrocarbons, supplied by Mieuxa, synthetic wax furnished by Sigma Aldrich, sodium chloride furnished by Sigma Aldrich and deionized water. The carbon chain distribution of the wax, shown in Fig. 2, was measured by the gas chromatography technique.

The wax appearance temperature (WAT) of the model oil (oil with wax) was determined using differential scanning calorimetry (DSC). Measurements at atmospheric pressure were performed with a Mettler Toledo DSC 1 system on samples weighing 10 to 15 mg, cooled from 80°C to −80°C at 5°C/min (Fig. 3). Under pressure, WAT was measured using a Setaram Micro DSC VII on samples of approximately 200 mg, cooled from 70°C to −40°C at 0.5°C/min (Fig. 3b). Here, a lower cooling rate is applied to ensure both thermal and chemical equilibrium during the cooling process. It is also worth noting that the sample mass used in the Micro DSC is approximately 20 times greater than that used in the Compact DSC, which further justifies the need for a slower cooling rate. The gas used to pressurize the system was the same as that applied in the flow loop, as shown in Table 2. Fig. 3b shows that pressurization with natural gas decreases the WAT. This effect occurs because the gas dissolves into the oil phase, causing oil expansion and consequently reducing the effective wax content.

Table 2
Composition of the natural gas mixture used in the experiments carried out in this work.

Component	Chemical formula	Mole fraction [%]
Methane	CH_4	91.7
Ethane	C_2H_6	5.9
Nitrogen	N_2	0.8
Carbon Dioxide	CO_2	0.8
Propane	C_3H_8	0.6
Butane	C_4H_{10}	0.1
Isobutane	$i-C_4H_{10}$	0.1

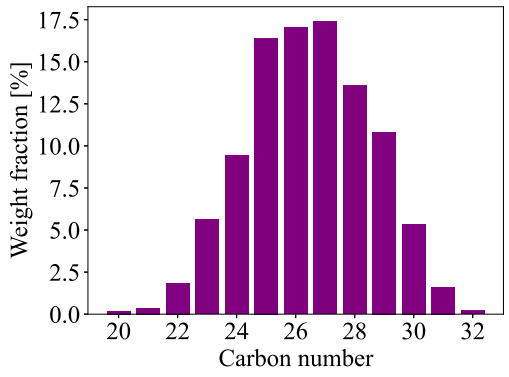

Fig. 2. Carbon chain distribution for the wax obtained by chromatography analysis.

Fig. 4 presents the Wax Precipitation Curve (WPC) calculated from data acquired using the DSC Compact at atmospheric pressure. The amount of precipitated wax corresponding to each wax content at 4 °C, the working temperature of the flow loop experiment, is highlighted. It is evident that the amount of precipitated wax increases as the temperature decreases. However, it can be observed that a small increase in wax content causes a disproportionately larger increase in the fraction of wax precipitated.

The viscosity of pure Kerdane and of the employed model oil (Fig. 5) was measured at 4 °C (working temperature of the flow loop) and atmospheric pressure by a rheometer MCR 302 by Anton Paar. Samples were cooled at a rate of 5 °C/h under an imposed shear rate of $10\,s^{-1}$. When the temperature is stable, 20 points were recorded during the shear rate ramp down from 1000 to $10\,s^{-1}$. As shown in Fig. 5, wax increases in the apparent viscosity and also changes the rheological behavior from Newtonian to shear thinning.

2.2. Procedure

Wax was dissolved in oil by heating and stirring at 40 °C for at least one hour before injection into the flow loop. Then, the experimental procedure carried out in this work is the same as the procedure applied in previous studies with the Archimede flow loop (De Almeida et al., 2023). It consists of six main steps, as illustrated in Fig. 6:

1. Control the temperature of the apparatus to 8 °C under flow (100 L/h);
2. Increase the flow rate to the required one (200 or 400 L/h);
3. Slowly pressurize to 8 bar using the gas compensation system;
4. Cool down the system to 4 °C;
5. Rapidly (manually) pressurize the system to 75 bar;
6. Set the gas compensation system to keep the pressure constant at 75 bar.

The model used to calculate the hydrate volume fraction, Eq. (1), and the water conversion, Eq. (2), was proposed by De Almeida (De Almeida et al., 2023).

$$\alpha_H = \frac{V_H}{V_H + V_W + V_O} \tag{1}$$

$$k_W = \frac{m_W^0 - m_W^t}{m_W^0} \tag{2}$$

where V $[m^3]$ stand for volume, m $[kg]$ stands for mass, α [-] stands for phase fraction and k [-] for conversion. The subscripts O, W, H refer to oil, water, and hydrate phase, respectively. The superscripts 0 and t stand for initial time (pressurization to 75 bar) and the time in analysis, respectively.

The model is based on a mass balance and volume conservation of water, oil, hydrates, and consumed gas. Hence, the hydrate volume

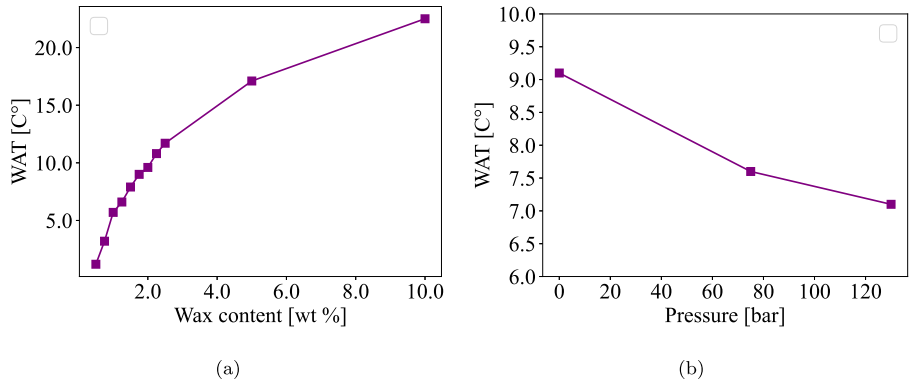

Fig. 3. Measured WAT as a function of: (a) wax content, measured at the DSC Compact at 5 °C/min cooling rate; (b) pressure, measured at the Micro DSC at a fixed wax content (2 wt %) measured at 0.5 °C/min cooling rate.

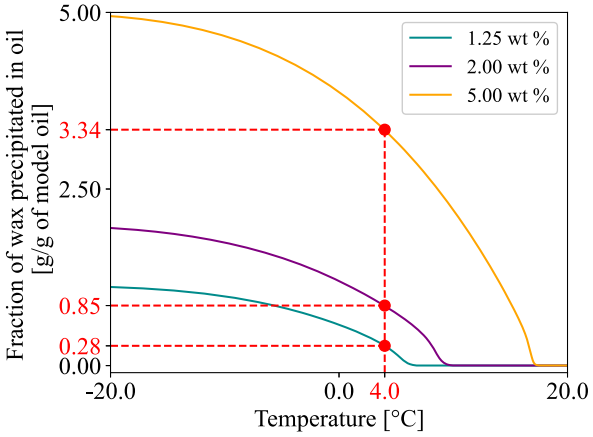

Fig. 4. Wax precipitation curve for model oil at 1.25 wt %, 2.00 wt % and 5.00 wt %, calculated from DSC measurements assuming a constant enthalpy of crystallization equal to 130 J/g.

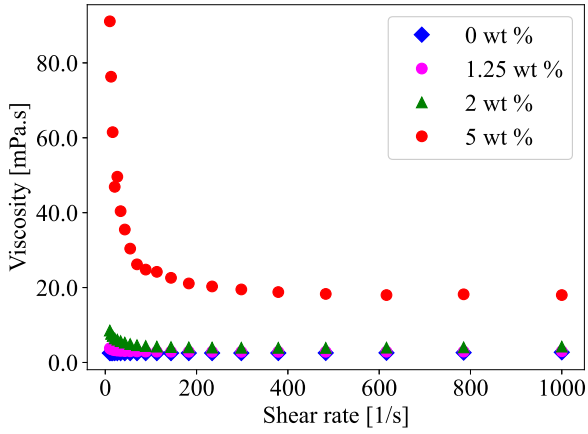

Fig. 5. Viscosity curve measured at 4 °C and ambient pressure for pure Kerdane (0 %) and Kerdane with 1.25, 2 and 5 wt % of wax.

fraction, or water conversion, is calculated from the absolute pressure, average temperature, mass of injected gas, density, and hydration number, adopting the following assumptions:

- Before the pressurization to 75 bar, the oil is saturated with the gas components;
- Gas dissolution into the oil does not occur during the fast pressurization; all injected gas contributes solely to increasing system pressure. Dissolution begins only after this step, when the gas compensation system is activated;
- The mass of dissolved gas in the oil phase is constant after the onset of hydrate formation;
- The fraction of each gas component being consumed to form hydrates is proportional to its molar fraction in the free gas;
- The hydrate's density is constant and equal to 910 g/L (approximately the density of methane hydrate Sloan and Koh (2007));
- The hydration number is 6.0. This assumption is based on experimental data from Ushida et al. Uchida et al. (1999). Their study demonstrated that the hydration number for methane hydrate remains approximately 6.0 under temperature and pressure conditions similar to those applied in this work.;
- The oil density and the concentration of gas dissolved in oil are assumed not to be significantly altered by wax.

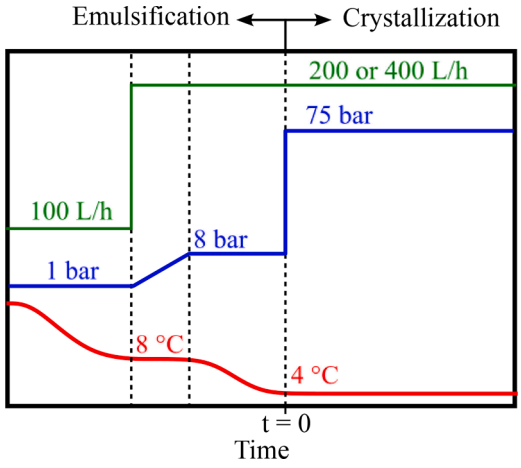

Fig. 6. Illustration of the experimental procedure adopted at the flow loop.

The mass balance from the hydrate onset (superscript *0*) to a time t, is given by:

$$m_G^0 + m_G^{inj,t} + m_W^0 = m_G^t + m_W^t + m_H^t \tag{3}$$

where $m_G^{inj,t}$ represents the mass of gas injected by the gas compensation system from the hydrate onset to the time t, whereas subscripts G, W, H refer to gas, water, and hydrate phase, respectively. Moreover, conservation of volume in the flow loop holds, namely:

$$V_G^0 + V_W^0 = V_G^t + V_W^t + V_H^t \tag{4}$$

Gas density is calculated using the Soave-Redlich-Kwong (SRK) equation of state, which provides accurate predictions for gases and

hydrocarbons when used with the appropriate binary interaction parameter (Kontogeorgis and Folas, 2009). Oil density is determined from the amount of dissolved gas, based on experimental correlations (De Almeida et al., 2023). The density of saline water was calculated as 1023.8 g/L, with its variation due to pressurization considered negligible.

By combining mass balance, volume conservation, and the known densities of each phase, a system of equations is established to calculate phase volumes. This enables the determination of the hydrate volume fraction (Eq. (1)). Further details on the model and calculation procedure can be found in De Almeida et al. (2023).

2.3. Experimental conditions

All experiments were performed with 10 % water cut. A low water cut was selected to investigate an oil-dominated system. Wax content is varied as: $(0; 1.25; 2; 5)$% wt. The wax-free scenario is as a reference. Wax content is defined as the weight fraction of wax to Kerdane, while the water cut is defined as the ratio of water volume to the total liquid volume, $WC = V_w/V_{tot}$.

Two flow rates are studied: 200 L/h and 400 L/h. These values were chosen to represent the widest possible operational range of flow rates in the flow loop. Since the apparent viscosity of the multiphase flow changes with the crystallization of wax (when $T <$ WAT) and with formation of hydrates (when $P = 75$ bar along with $T = 4$ °C), the Reynolds number of the initial flow (ambient conditions) is computed, considering the viscosity and the density of the oil phase, corresponding to the two studied flow rates. The Reynolds numbers are $Re = 2300$ and $Re = 4533$ for the lower and higher flow rate, respectively.

3. Results and discussion

A summary of all experiments and key outcomes (plugging, water conversion, hydrate fraction, and time to plug) is presented in Table 3. Each experiment is performed at least twice to ensure confidence in the data.

The discussion is divided into three parts. First, the emulsion properties before hydrate formation are discussed. Then, the evolution of the hydrate slurry, with and without wax, at both studied flow rates is analyzed. Finally, the effects of wax on hydrate formation and transportability are discussed.

3.1. Monitoring wax appearance

The experimental protocol implies first reducing the temperature of the flow loop and then pressurizing with natural gas (see Fig. 6). Wax precipitation begins as the temperature drops below the WAT. The pressurization with natural gas causes gas dissolution into the oil, swelling the oil phase, consequently decreasing the relative wax content, as shown in Fig. 3b. Since the larger the wax content, the larger the mass of precipitated wax, part of the wax may redissolve into the oil with the pressurization. This phenomenon is illustrated in Fig. 7, where it is shown, for the experiment #7, the horizontal pressure drop (blue line) and the average temperature (green line), the chords count, and PVM images. The average temperature is defined as $\Sigma_{i=1}^{n=9} T_i/n$ with n the number of temperature probes.

When $T =$ WAT (left vertical dashed line in Fig. 7(a)), it is possible to notice an increase in pressure drop and in the counts of the FBRM, along with the appearance of waxy structures in the PVM images. As the temperature decreases further, the apparent viscosity of the oil increases due to both greater wax precipitation and the inherent rise in oil viscosity at lower temperatures, which contributes to a higher pressure drop. When the system is pressurized to 75 bar (right vertical dashed line in Fig. 7(a)), gas dissolves into the oil, reducing its viscosity and contributing to decreasing the pressure drop, and the counts from FBRM. Therefore, the aforementioned effects are not solely due to wax precipitating/redissolving in the oil phase, but rather a combined effect of oil viscosity caused by gas dissolution, wax precipitation, and temperature variation.

3.2. Study of the emulsion before hydrate formation

After pressurization, the system enters the hydrate stability region. The continuous phase and the flow structures of the emulsion before hydrate formation are identified through the permittivity probe and high-speed camera. At 4 °C, the dielectric of the Kerdane oil is equal to 2.7, while the dielectric of the water with 30 g/L of NaCl is equal to 87.9 (De Almeida et al., 2023). This difference allows for identifying the continuous phase. Fig. 8 presents the temporal evolution of the permittivity of the emulsion along with one corresponding flow image acquired by the high-speed camera for the experiments 1, 4, 11, and 13 of Table 3.

For all cases, the measured permittivity oscillates near the permittivity of the oil, suggesting that oil is the continuous phase. In addition, for the images acquired at 200 L/h, Fig. 8(a) and (c), the droplets

Table 3
Summary of experimental results. Wax content is measured as mass fraction relative to the mass of the oil. Water conversion is calculated as a mole percentage at the final time of the experiment. The hydrate fraction is calculated as a volume percentage at the final time of the experiment. Time to plug is defined as the time elapsed between the hydrate onset and the plug or the end of the experiment if plug the did not occur.

Exp.	Wax content [wt %]	Flow rate [L/h]	Plug	Water conversion [%]	Hydrate fraction [%]	Time to plug [min]
#1	0	200	No	67.3	8.0	172
#2			No	39.9	4.8	91
#3			Yes	56.3	7.1	354
#4		400	No	72.7	9.1	225
#5			Yes	65.0	8.0	228
#6	1.25	200	Yes	42.0	5.1	206
#7			Yes	45.4	5.5	183
#8		400	Yes	51.3	6.3	226
#9			Yes	55.5	6.9	216
#10			Yes	59.3	7.5	292
#11	2.00	200	No	36.6	4.4	273
#12			No	28.0	3.4	245
#13		400	No	31.3	3.9	191
#14			No	12.3	1.5	303
#15	5.00	200	No	22.0	2.7	126
#16			No	-	-	-
#17		400	No	9.3	1.1	112
#18			No	20.0	2.5	134

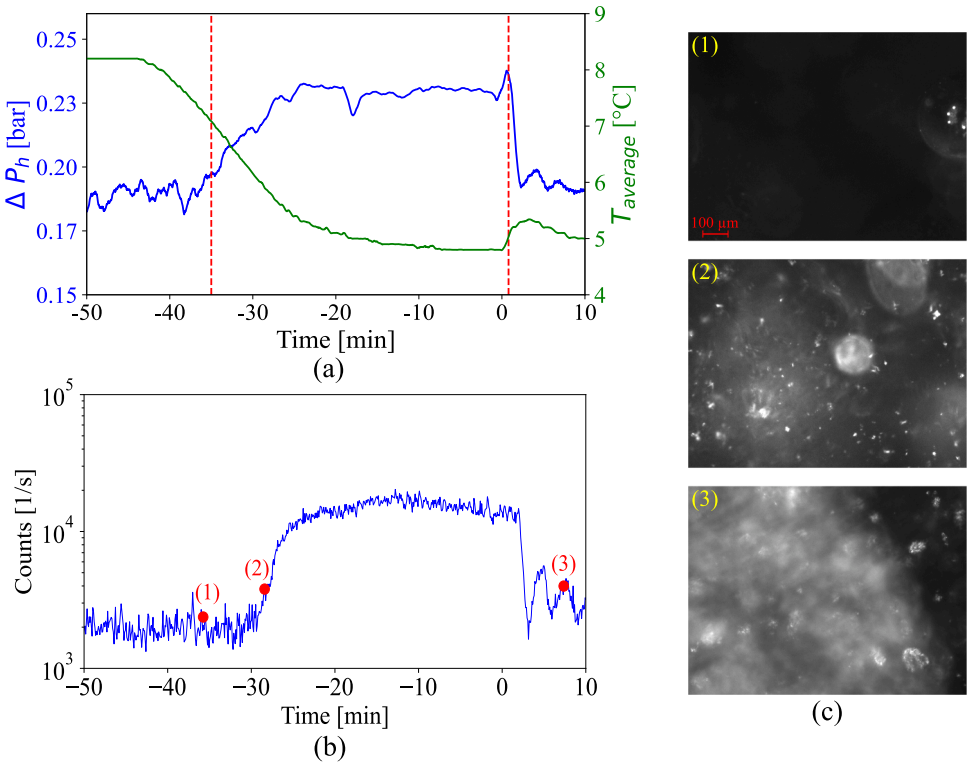

Fig. 7. Wax appearance detection through different probes: (a) horizontal pressure drop and temperature over time, where the left vertical dashed line represents when the system reaches the WAT and the right vertical dashed line represents the pressurization to 75 bar, (b) FBRM total counts and (c) PVM images for experiment at 1.25 wt % wax content and 200 L/h (experiment #7 in Table 3). Points 1, 2, and 3 in figure (b) represent the time of PVM images 1, 2, and 3 in figure (c).

are preferentially at the bottom of the pipeline, confirming that the continuous phase is oil and the dispersed phase is water as oil is lighter than water.

Moreover, the permittivity signal shows a higher heterogeneity of the flow at 200 L/h, caused by the passage of large droplets. As expected, increasing the flow rate to 400 L/h (Fig. 8b and d), droplet size and heterogeneity reduce, causing the signal to present fewer fluctuations and smaller peaks.

Interestingly, at 200 L/h, the peaks observed in the system containing wax (Fig. 8c) are about twice as large as the peaks of the wax-free system (Fig. 8a). As shown by De Almeida et al. (2023), higher dielectric can be correlated to a higher local water cut, suggesting that the droplets are larger in the presence of wax. HSC images taken during the final 60 s before hydrate formation were analyzed to quantify droplet size. The results, summarized in Table 4, confirm that average droplet diameter increases with wax content at both flow rates. Measurements were not performed for the 5 wt% wax case due to optical limitations caused by the high wax concentration.

This behavior has been observed in previous experimental studies where droplet size increases with viscosity up to a certain threshold (Pandolfe, 1981).

Table 4
Average droplet diameter, in millimeters, measured from the images acquired by the high-speed camera during the last 60 s before hydrate nucleation. The confidence interval is calculated based on the critical value from Student's t-distribution and the standard error, based on a confidence level of 95 %. The Procedure is explained in the Appendix A.

Flow rate [L/h]	Wax content [wt %]		
	0	1.25	2
200	0.94 ± 0.08	1.06 ± 0.11	1.35 ± 0.10
400	0.51 ± 0.03	0.59 ± 0.05	0.71 ± 0.04

The variation in the droplet diameter is due to the higher viscosity of the waxy oil compared to the pure oil (Fig. 5) (Habchi et al., 2009). The maximum stable diameter, $d_{\max}$, arises from the energy balance between the turbulent kinetic energy and the droplet surface energy (Hinze, 1955; Brauner, 2001), namely:

$$\frac{\rho_c u'^2}{2} \propto \frac{4\sigma_i}{d_{max}} \tag{5}$$

where ρ_c $[kg/m^3]$ is the density of the continuous phase, u' $[m/s]$ is the fluctuating velocity and σ_i $[kg/s^2]$ is the surface tension.

The fluctuating velocity is related to the Reynolds number. Thus, by increasing the flow rate, and therefore increasing the Reynolds number, the droplet size reduces. It turns out that wax increases the apparent viscosity, consequently reducing the Reynolds number (considering only the continuous phase), and resulting in larger droplets. For this, it is assumed that surface tension is not greatly affected by wax (Chen et al., 2021).

3.3. Study of the hydrate slurry flow

The onset of hydrate formation is detected by all the probes. Due to the sensitivity of each probe and the local nature of the phenomenon, they do not detect hydrates at the same time. Therefore, hydrate onset is defined as the time at which the first probe detects its presence, regardless of the location or the type of the probe. Fig. 9 shows how different probes react to hydrate onset for the experiment #5: the average temperature and the chord counts (FBRM) in the top panel; the horizontal pressure drop and the density (Coriolis) in the middle panel; the absolute energy (AE) signals in the bottom panel. The location of the hydrate onset can be detected through this analysis. In this example, hydrate onset is first detected by the acoustic emission probe 2A, which is located at the first loop of the horizontal section, after the downward section (Fig. 1).

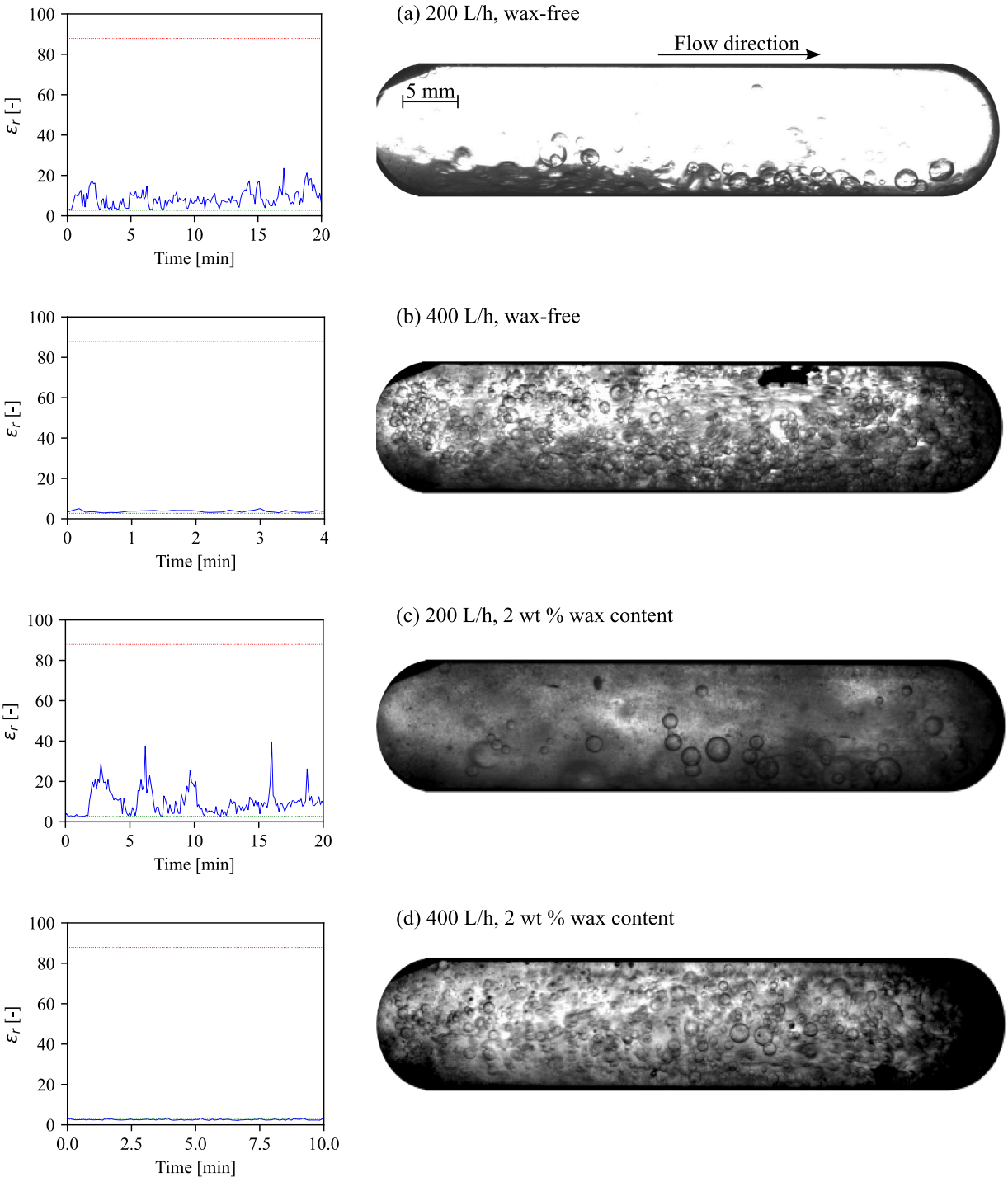

Fig. 8. Analysis of the emulsion before hydrate formation using permittivity (left) and flow images from the high-speed camera (right), for the experiments 1, 4, 11, and 13 (from top to bottom, respectively) in Table 3.

Hydrate formation increases fluid viscosity, which consequently increases the pressure drop (blue line in Fig. 9(b)). Also, due to the exothermic nature of the crystallization process, a slight temperature increase is observed at the onset (blue line in Fig. 9(a)). The nucleation of hydrate particles creates new interfaces, affecting the chord counts of the FBRM (green line in Fig. 9(a)). In addition, solid particles can collide among themselves and/or with the wall, releasing acoustic energy in the flow, detected by the acoustic emission probes (Fig. 9(c)).

After the detection of the onset, the temporal evolution of the slurry flow is monitored. As can be seen in Fig. 10 for experiment 3, the chart can be divided into three sections: (1) before hydrate onset; (2) hydrate transport; and (3) hydrate aggregation and/or deposition. The first few minutes after the onset, density, absolute energy, and permittivity show a strong oscillation, suggesting the agglomeration of the hydrate particles, which are confirmed by the images of the high-speed camera (Fig. 11). Suddenly, all signal fluctuations diminish, indicating that a homogeneous flow takes place. At this point, hydrate aggregates either deposit or accumulate on some sections of the flow loop.

While the absolute energy in section (3) presents values similar to the section (1), the steady signal of the density in section (3) is lower than in

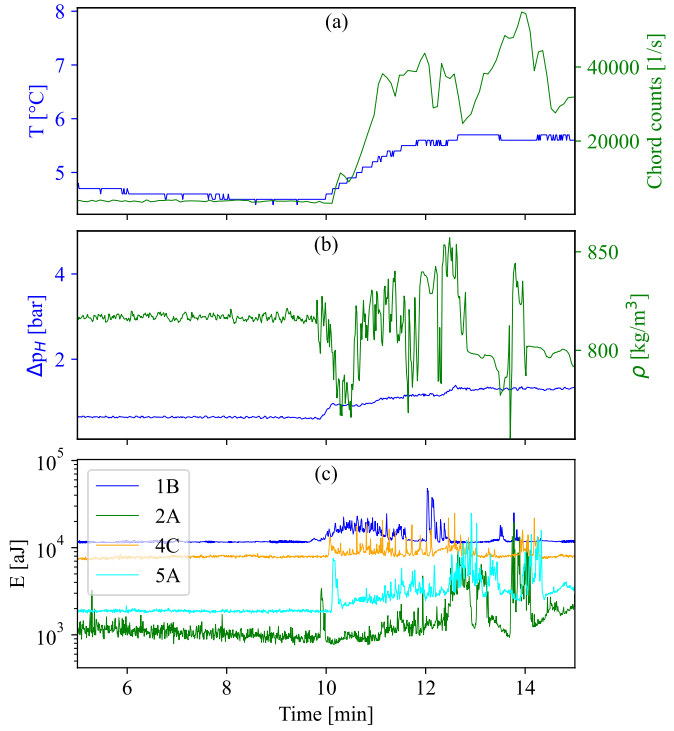

Fig. 9. Hydrate onset detection through (a) average temperature and chord counts, (b) horizontal pressure drop and density, and (c) AE absolute energy for experiment at 400 L/h without wax (#5).

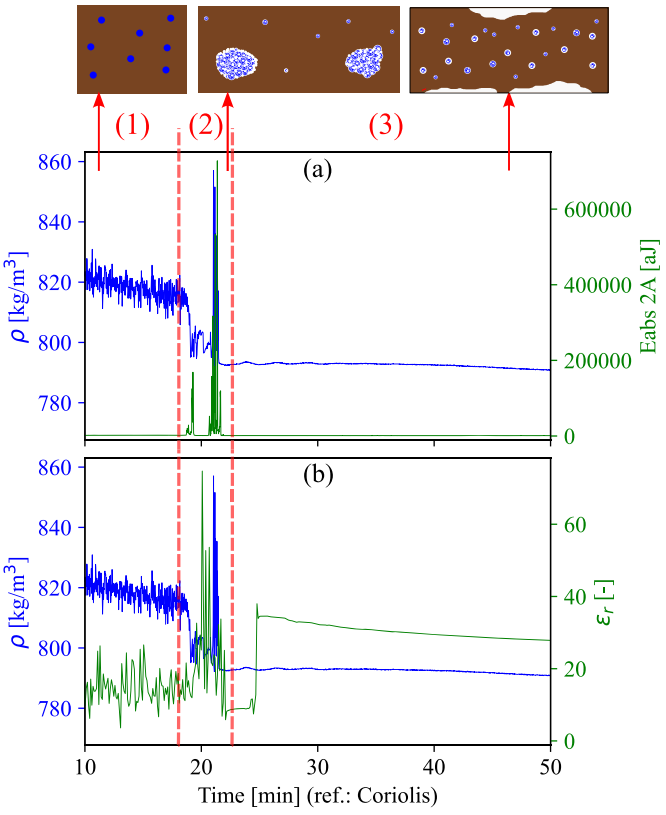

Fig. 10. Density, acoustic emission 2A and permittivity over time for experiment at 200 L/h without wax (experiment #3). At the top, a sketch of the flow is shown.

section (1). This indicates that the agglomerates that were in the bulk in section (2) have deposited in the flow loop. Meanwhile, hydrates have deposited on the PVM lens and high-speed camera window (not shown).

High-speed camera images show the passage of large aggregates shortly after hydrate onset (Fig. 11). Indeed, for this experiment, hydrates were detected after 17 min and 15 s. A few seconds later, hydrates have already started to agglomerate.

The first few min after hydrate formation, hydrate particles are agglomerating and, when the apparent weight (weight minus buoyancy) overcomes the lift forces generated by the flow, they settle down, forming a bed. Since steel is hydrophilic, if the hydrate bed stays time enough in contact with the wall, it can consolidate to the wall, forming a deposit. This deposit creates a restriction to the flow, increasing the pressure drop. At larger flow rates, this effect is less noticeable, as shear stress limits the size of agglomerates, resulting in less deposition and more dispersed particles in the bulk.

Later, after minute 27, the hydrate deposit builds up gradually over time, increasing the pressure drop, as shown in Fig. 12. The deposit eventually breaks, leading to a decrease in the pressure drop and releasing particles that are detected by the acoustic emission (Fig. 12(a)). In Fig. 12(b), signals from acoustic emission probes in the horizontal section are shown for the highlighted section in Fig. 12(a). The sequential detection of these particles released from the deposits, visible in Fig. 12(b), indicates their movement in the horizontal section (see Fig. 1 for the location of AE probes). Also, when particles are flowing in the bulk, both the active area for crystallization and the water squeezing - i.e., water squeezing out from the hydrate particle as the porous are closing in time - increases (Bassani, 2020), re-activating the crystallization process. As can be seen in Fig. 12(c), the discontinuities in the hydrate fraction of the system are synchronized with the sharp decreases of the horizontal pressure drop, indicating that the breakage of the deposit reinitiates crystallization.

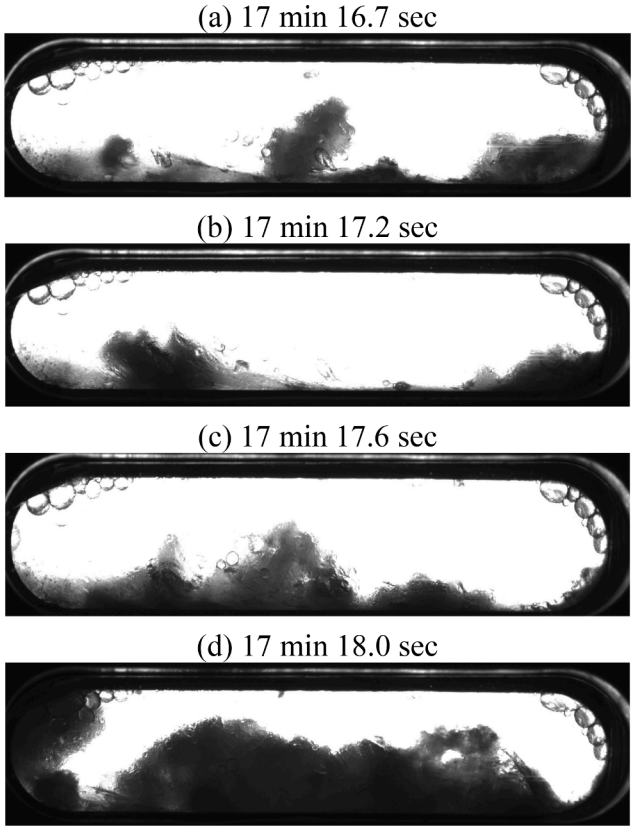

Fig. 11. High speed camera images of experiment at 200 L/h without wax (#3) after hydrate detection (17 min 15 sec).

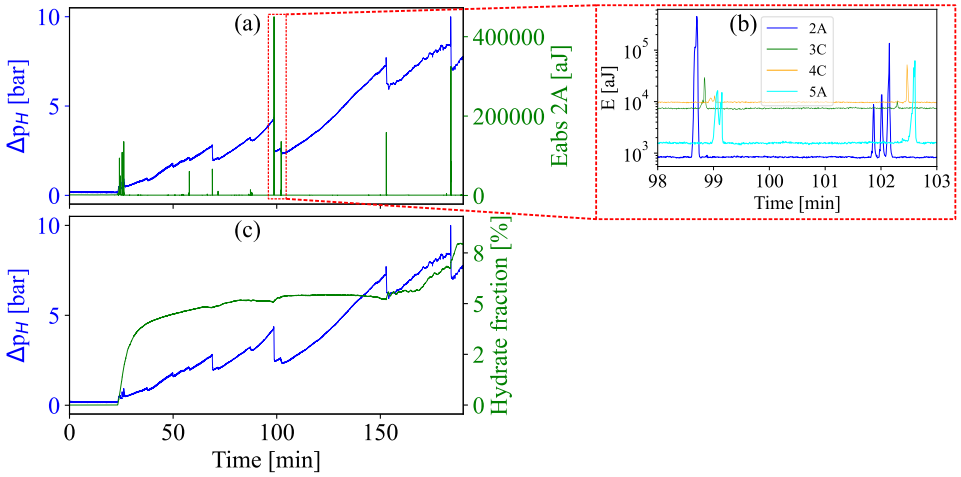

Fig. 12. Experimental data suggesting breakage of deposit and restart of crystallization process for experiment at 200 L/h without wax (#1). (a) Horizontal pressure drop and absolute energy (2A) over time. (b) Absolute energy from probes 2A, 3C, 4C and 5A over time. (c) Horizontal pressure drop and hydrate fraction over time.

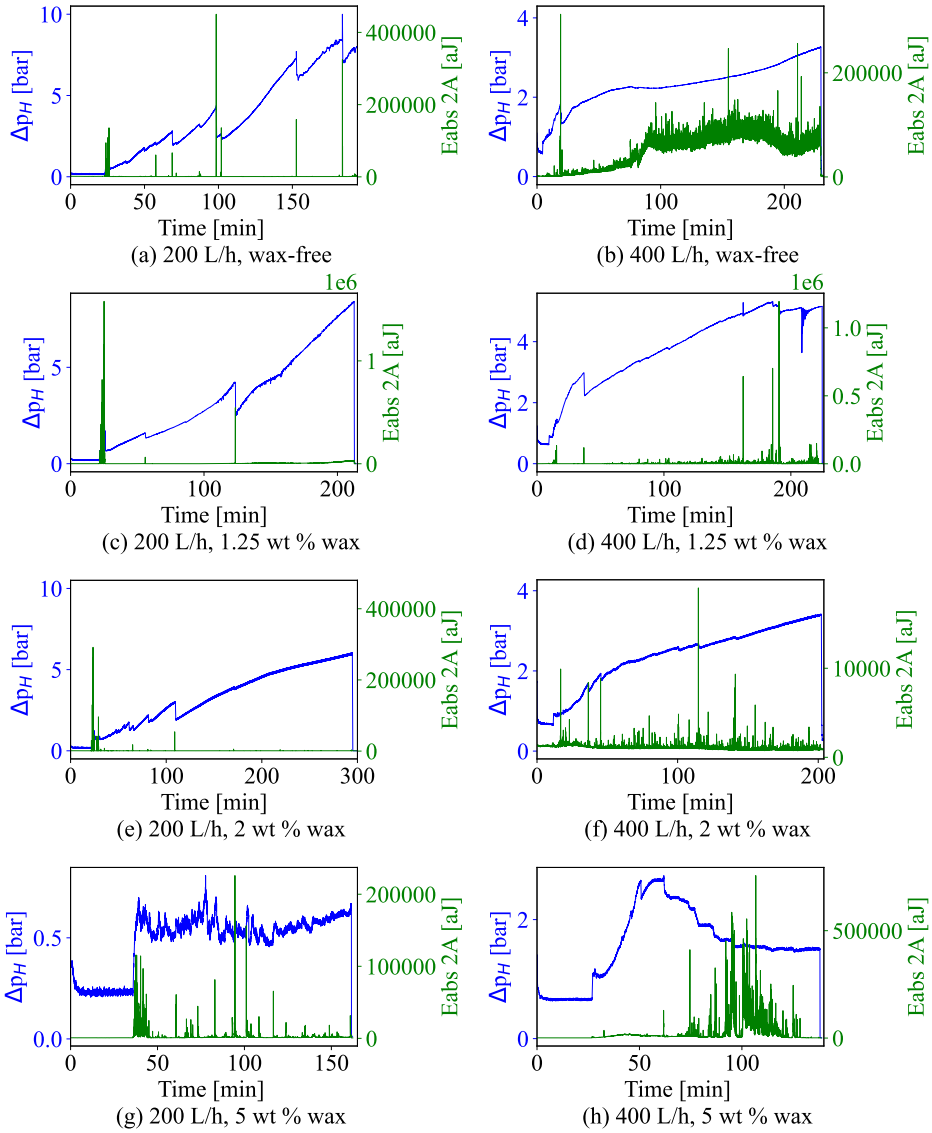

Fig. 13. Horizontal pressure drop and absolute energy (2A) for experiments at (a) 200 L/h and wax-free (experiment #1), (b) 400 L/h and wax-free (#4), (c) 200 L/h and 1.25 wt % of wax content (#7), (d) 400 L/h and 1.25 wt % of wax content (#9), (e) 200 L/h and 2 wt % of wax content (#11), (f) 400 L/h and 2 wt % of wax content (#13), (g) 200 L/h and 5 wt % of wax content (#15), and (h) 400 L/h and 5 wt % of wax content (#17).

3.4. Effect of wax on hydrate formation

The aforementioned mechanisms are also observed at the higher flow rate and in the presence of wax. As shown in Fig. 13, pressure drop trends over time are similar across varying flow rates and wax contents, with sharp reductions in pressure drop typically synchronized with peaks in acoustic energy (probe 2A). The exception to this trend is the system at 5 wt % of wax at both flow rates, depicted in Fig. 13(g), and (h).

At 200 L/h and 5 wt % of wax (Fig. 13g) the pressure drop increases after hydrate formation, as it also happens at lower wax content (Figs. 13a, c, and e). However, unlike the cases with lower wax content, the pressure drop at 5 wt % of wax does not increase steadily over time. Instead, it oscillates around a higher baseline, suggesting a heterogeneous flow where hydrate beds intermittently detach and are transported by the flow, causing fluctuations in pressure drop (Bassani, 2020).

At 400 L/h and 5 wt % of wax (Fig. 13h), the pressure drop also behaves differently as it happens at lower wax content. Indeed, it initially grows, and then decreases to finally stabilize. As for the previously discussed scenario (200 L/h), a flow restriction created by a deposit is not expected here. However, since the pressure drop does not oscillate, a more homogeneous flow is anticipated, in line with the higher Reynolds number.

Furthermore, analysing the absolute energy in different wax contents and different flow rates (Fig. 14), one notes that at low flow rate the behavior is similar with and without wax, with the signal presenting some local peaks related to the passage of some aggregates. Conversely, at 400 L/h, there is a significant difference between the signals obtained from the experiment with and without wax. Indeed, after hydrate formation, the absolute energy gradually increases for the wax-free experiment and for the case at 1.25 wt % of wax, while the 2 wt % curve presents a behavior similar to 200 L/h, where the curve barely deviates from its baseline with some local peaks. This indicates that at 400 L/h without wax the flow is more homogeneous, keeping particles suspended and distributed, while for the wax-containing case the flow seems more heterogeneous (local peaks in the absolute energy), resulting from agglomeration. As shown by De Almeida et al. (2022), the absolute energy tends to be higher in the presence of hydrates in the bulk.

From no wax up to 2 wt %, as the wax content increases, the absolute energy decreases as fewer hydrates are transported in the system and more agglomeration and deposition occur. The scenario at 5 wt % (curve cyan in Fig. 14) does not follow this trend. Indeed, at both flow rates, it presents higher levels of energies, even though a lower hydrate fraction is involved. The reason for this is that this scenario is affected by a much higher precipitated wax content than the others (Fig. 4), which results in more wax deposition during the cooling stage of the experimental protocol. Since wax is hydrophobic while hydrate is hydrophilic, the wax layer developed on the pipeline walls prevents the consolidation of a deposit.

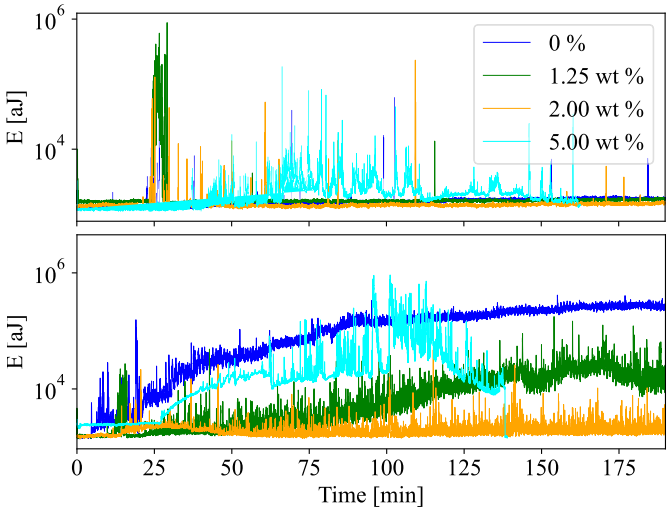

Fig. 14. Absolute energy (5A) over time comparing experiment with and without wax at (a) 200 L/h (#1, #6, # 11 and # 15) and (b) 400 L/h (#4, #10, #13 and #17).

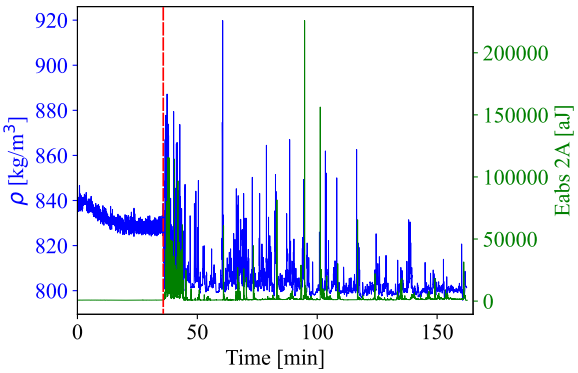

Fig. 15. Density and absolute energy (probe 2A) over time for experiment at 200 L/h and 5 wt % (#15). The dashed red line represents hydrate onset.

In addition, the apparent viscosity of the oil phase in this condition is much higher (Fig. 5), resulting in a lower Reynolds number (i.e. at 400 L/h, Reynolds number calculated for the oil phase decreases from 4533 to 630 when 5 wt % of wax is added to the system) and, as a consequence, less collisions among the particles, which in turn prevents agglomeration encouraging the particles to remain suspended in the bulk. The combination of those effects explains the higher acoustic energy of the scenario at 5 wt %, although it contains less hydrate and is less turbulent. The presence of particles flowing in such a system can be proved by analysing the density and the acoustic emission. As can be seen in Fig. 15, after hydrate formation, both density and absolute energy present a noisy behavior, as shown earlier in the analysis of Fig. 10. However, unlike the scenarios without wax (Fig. 10), the signals remain noisy throughout the experiment, indicating the passage of hydrate particles.

Also, the wax layer formed during the cooling stage can be verified by the temperature profile after hydrate formation, shown in Fig. 16. Due to the exothermic nature of the crystallization process, a peak is noticeable in the temperature signal at the moment of the hydrate onset. However, while for the wax-free system (blue curve in Fig. 16) and for the scenario with 1.25 wt % (green curve in Fig. 16) the temperature returns to its level before hydrate formation, at higher wax content

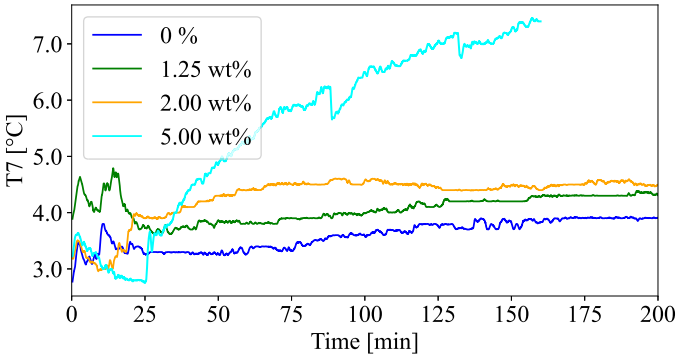

Fig. 16. Temperature (T_7) over time for experiments at 400 L/h and wax-free (#4), 1.25 wt % (#10), 2.00 wt % (#13) and 5.00 wt % (#18) of wax content.

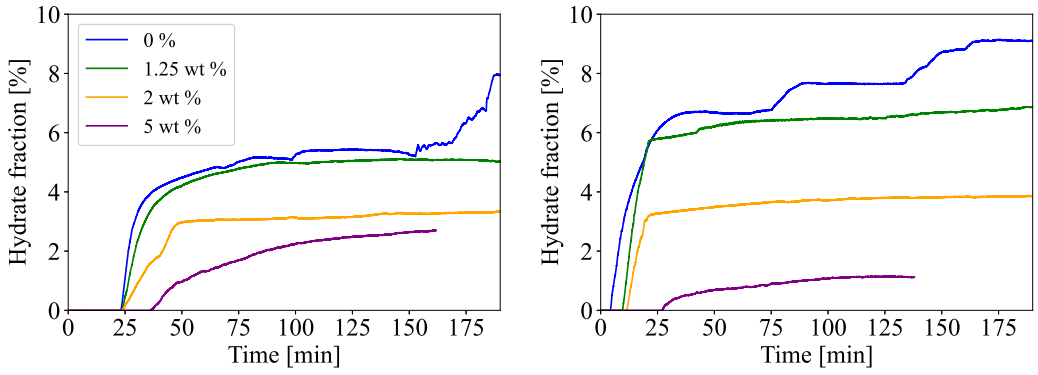

(a) 200 L/h (b) 400 L/h

Fig. 17. Hydrate fraction over time comparison for experiments with and without wax at (a) 200 L/h and (b) 400 L/h.

Table 5
Reynolds number computed considering oil single-phase flow, oil density at ambient conditions, internal diameter of the horizontal section, and viscosity measured at ambient conditions.

Reynolds number		
Wax content [wt %]	Flow rate [L/h]	
	200	400
0	2266	4533
1.25	2023	4047
2.00	1416	2833
5.00	315	630

(orange and cyan curves in Fig. 16) the temperature is larger than the starting configuration, indicating thermal insulation caused by wax deposits.

To investigate the effect of wax on the hydrate formation and plugging risk, Fig. 17 shows the temporal evolution of the hydrate fraction (or water conversion) by varying the wax content, at low (left panel) and high (right panel) flow rate. It is noteworthy that, at both flow rates, the hydrate fraction is significantly lower in the presence of 2 and 5 wt % of wax. Moreover, analysing the data summarized in Table 3, one can notice that those experiments did not plug.

On the contrary, at 1.25 wt %, wax content, the hydrate fraction is similar to the case of the wax-free system. Indeed, for this scenario, the amount of wax precipitated calculated from the thermal analysis is 0.28 wt %, while at 2 wt % wax content it is 0.85 wt %, as shown in Fig. 4. This explains the behaviour of the 1.25 wt % wax-content system relative to the wax-free system. In addition, one should note that the WAT measurements are made under atmospheric pressure, thus, the measured precipitated wax should be even lower when the system is pressurized with natural gas (Vieira et al., 2008; Sousa et al., 2023).

To conclude, at 10 % water cut wax crystallization in the oil has the effect of slowing down the water conversion and decreasing the hydrate fraction in the flow. As a consequence, the plugging of the system is hindered by the presence of wax. With reference to Fig. 5, this can be explained as follows:

1. at molecular scale, wax increases the viscosity of the oil, which decreases the Reynolds number;
2. at micron scale, the decreased Reynolds number leads to a decrease in turbulent kinetic energy content;
3. at millimetric scale, the less turbulent kinetic energy of the system increases agglomeration;
4. at flow loop scale, the increased agglomeration leads to a decrease in the active surface for crystallization, which contributes to ceasing the water conversion. Moreover, when beds are formed or when they consolidate to the wall, it decreases or ceases the water permeation in the hydrate particle, which also contributes to reducing or ceasing the water conversion (Bassani, 2020).

This mechanism is also proved by the images shown in Fig. 8, where the size of the droplets is related to the turbulent kinetic energy, which is related to the Reynolds number. As shown in Table 5, the Reynolds number decreases with increasing wax content. At a flow rate of 200 L/h, the flow transitions from transitional to laminar, while at 400 L/h, it shifts from turbulent to laminar as the wax content increases. Bigger droplets prove that the shear is lower in the presence of wax, which, after hydrate formation, contributes to more agglomeration in the system. In turn, bigger droplets reduce the active surface for crystallization, contributing to a lower hydrate fraction.

4. Conclusions

In this work, an experimental campaign using a high-pressure flow loop was conducted to investigate the effect of wax concentration on hydrate formation in a water-in-oil flow, where the water content represents 10 % of the total liquid volume.

The results indicate that the primary effect of wax is to reduce water conversion. The presence of wax increases the apparent viscosity of the slurry, which lowers the Reynolds number. This, in turn, affects the emulsion droplet size and, after hydrate formation, the agglomeration of particles. The formation of aggregates, and consequently beds (settled agglomerates) or deposits, reduces the available surface area for crystallization. As a result, water conversion is lower compared to the wax-free case.

Under these conditions, the presence of wax hinders pipeline plugging, to the extent that at sufficiently high wax concentrations, plugging is prevented altogether, regardless of the flow rate.

CRediT authorship contribution statement

Luiz Henrique Meneghel Lino: Writing - original draft, Visualization, Methodology, Investigation, Formal analysis, Data curation; **Gianluca Lavalle:** Writing - review & editing, Formal analysis; **Eric Serris:** Writing - review & editing, Resources, Formal analysis; **Jean Michel Herri:** Supervision, Project administration; **Ana Cameirao:** Writing - review & editing, Supervision, Project administration, Formal analysis, Conceptualization; **Nicolas Lesage:** Writing - review & editing, Supervision, Formal analysis; **Annie Fidel Dufour:** Writing - review & editing, Supervision, Project administration, Formal analysis.

Data availability

The authors do not have permission to share data.

Declaration of competing interest

The authors declare the following financial interests/personal relationships which may be considered as potential competing interests:

Luiz Henrique Meneghel Lino reports financial support was provided by TotalEnergies SE. If there are other authors, they declare that they have no known competing financial interests or personal relationships that could have appeared to influence the work reported in this paper.

Appendix A. Uncertainties

A precision balance, Precisa, model IDK 18 000 D, with both the readability and the repeatability equal to 0.1 g. Considering the additive influence of the repeatability and the readability (Salahinejad and Aflaki, 2007), applying the uncertainty and error propagation Vuolo (1996) and assuming a Gaussian distribution and a confidence level of 95 %, the expanded uncertainty on the water cut is ±0.03 %, on the salt concentration is ±0.94 %, and on the wax content is ±0.3 %. The Coriolis presents an uncertainty of ±0.2 % measuring the liquid flow rate, and ±2.0 kg/m^3.

The confidence interval for the droplet diameter is calculated as follows:

1. The mean, $\overline{x}$, of observations, n, is calculated by $\overline{x} = \sum_{i=1}^{n} x_i/n$;
2. Then, the standard deviation, s, is computed as follow:

$$s = \sqrt{\frac{\sum_{i=1}^{n}(x_i - \overline{x})^2}{n}}$$

3. Applying a confidence level of 95 % and the degrees of freedom (n – 1), the critical value, c, of the t-Student distribution is obtained;
4. Finally, the confidence interval is given by:

$$\left[\overline{x} + \frac{cs}{\sqrt{n}}, \overline{x} - \frac{cs}{\sqrt{n}}\right]$$

References

Bassani, C.L., 2020. A Multiscale Approach for Gas Hydrates Considering Structure, Growth Kinetics, Agglomeration and Transportability under Multiphase Flow Conditions. Ph.D. thesis. Université de Lyon; Universidade Technologica Federal do Parana (Brésil).

Brauner, N., 2001. The prediction of dispersed flows boundaries in liquid–liquid and gas–liquid systems. Int. J. Multiphase Flow 27 (5), 885–910.

Chen, X., Sun, G., Liu, D., Zhang, H., Zhang, H., Li, C., Zhao, Z., 2021. Two effects of wax crystals on stabilizing water-in-oil emulsions. Colloids Surf., A.: Eng. Aspects 625, 126884.

Chen, Y., Shi, B., Liu, Y., Song, S., Gong, J., 2018. Experimental and theoretical investigation of the interaction between hydrate formation and wax precipitation in water-in-oil emulsions. Energy & Fuels 32 (9), 9081–9092.

Coutinho, J. A.P., Edmonds, B., Moorwood, T., Szczepanski, R., Zhang, X., 2002. Reliable wax predictions for flow assurance. In: SPE Europec featured at EAGE Conference and Exhibition?. SPE, pp. SPE–78324.

De Almeida, V., Serris, E., Cameirão, A., Herri, J.-M., Abadie, E., Glenat, P., 2022. Monitoring gas hydrates under multiphase flow in a high pressure flow loop by means of an acoustic emission technology. J. Nat. Gas Sci. Eng. 97, 104338.

De Almeida, V., Serris, E., Lavalle, G., Cameirão, A., Herri, J.-M., Abadie, E., Lesage, N., Dufour, A.F., 2023. Mechanisms of hydrate blockage in oil-water dispersions based on flow loop experiments. Chem. Eng. Sci. 273, 118632.

Fidel-Dufour, A., Gruy, F., Herri, J.-M., 2006. Rheology of methane hydrate slurries during their crystallization in a water in dodecane emulsion under flowing. Chem. Eng. Sci. 61 (2), 505–515.

Gao, S., 2008. Investigation of interactions between gas hydrates and several other flow assurance elements. Energy & Fuels 22 (5), 3150–3153.

Habchi, C., Ouarets, S., Lemenand, T., Della Valle, D., Bellettre, J., Peerhossaini, H., 2009. Influence of viscosity ratio on droplets formation in a chaotic advection flow. Int. J. Chem. Reactor Eng. 7 (1).

Hinze, J.O., 1955. Fundamentals of the hydrodynamic mechanism of splitting in dispersion process. AICHE J. 1 (3), 289–295.

Hong, J., Wang, Z., Wang, C., Zhang, J., Liu, W., Ling, K., 2025. Modeling of multiphase flow with the wellbore in gas-condensate reservoirs under high gas/liquid ratio conditions and field application. SPE J. 30 (3), 1–14.

Jing, J., Zhuang, L., Karimov, R., Sun, J., Zhang, X., 2023. Investigation of natural gas hydrate formation and slurry viscosity in non-emulsifying oil systems. Chem. Eng. Res. Des. 190, 687–703.

Kontogeorgis, G.M., Folas, G.K., 2009. Thermodynamic models for industrial applications: from classical and advanced mixing rules to association theories. John Wiley & Sons.

Leba, H., Cameirao, A., Herri, J.-M., Darbouret, M., Peytavy, J.-L., Glénat, P., 2010. Chord length distributions measurements during crystallization and agglomeration of gas hydrate in a water-in-oil emulsion: simulation and experimentation. Chem. Eng. Sci. 65 (3), 1185–1200.

Liu, Y., Meng, J., Lv, X., Ma, Q., Shi, B., Wang, C., Huang, H., Wu, C., Zhou, S., Song, S., 2022a. Investigating hydrate formation and flow properties in water-oil flow systems in the presence of wax. Front. Energy Res. 10, 986901.

Liu, Y., Shi, B., Ding, L., Ma, Q., Chen, Y., Song, S., Zhang, Y., Yong, Y., Lv, X., Wu, H., et al., 2019. Study of hydrate formation in water-in-waxy oil emulsions considering heat transfer and mass transfer. Fuel 244, 282–295.

Liu, Y., Shi, B., Ding, L., Yong, Y., Zhang, Y., Ma, Q., Lv, X., Song, S., Yang, J., Wang, W., et al., 2018. Investigation of hydrate agglomeration and plugging mechanism in low-wax-content water-in-oil emulsion systems. Energy & fuels 32 (9), 8986–9000.

Liu, Z., Geng, X., Gao, Y., Yao, H., Chen, H., Li, Z., Song, G., Wang, W., Li, Y., 2022b. Effect of wax crystal on the kinetic and morphology of gas hydrate deposition in water-in-oil emulsions. Fuel 330, 125501.

Ma, Q., Wang, W., Liu, Y., Yang, J., Shi, B., Gong, J., 2017. Wax adsorption at paraffin oil–water interface stabilized by span80. Colloids Surf., A: Eng. Aspects 518, 73–79.

Melchuna, A., Cameirao, A., Herri, J.-M., Glenat, P., 2016. Topological modeling of methane hydrate crystallization from low to high water cut emulsion systems. Fluid Phase Equilib. 413, 158–169.

Pandolfe, W.D., 1981. Effect of dispersed and continuous phase viscosity on droplet size of emulsions generated by homogenization. J. Dispers. Sci. Technol. 2 (4), 459–474.

Pham, T.-K., Cameirao, A., Melchuna, A., Herri, J.-M., Glénat, P., 2020. Relative pressure drop model for hydrate formation and transportability in flowlines in high water cut systems. Energies 13 (3), 686.

Salahinejad, M., Aflaki, F., 2007. Uncertainty measurement of weighing results from an electronic analytical balance. Meas. Sci. Rev. 7 (6), 1–9.

Shahnazar, S., Hasan, N., 2014. Gas hydrate formation condition: review on experimental and modeling approaches. Fluid Phase Equilib. 379, 72–85.

Shi, B.-H., Chai, S., Ding, L., Chen, Y.-C., Liu, Y., Song, S.-F., Yao, H.-Y., Wu, H.-H., Wang, W., Gong, J., 2018. An investigation on gas hydrate formation and slurry viscosity in the presence of wax crystals. AlChE J. 64 (9), 3502–3518.

Sloan, E.D., 2010. Natural gas hydrates in flow assurance. Gulf Professional Publishing.

Sloan, , E.D. Jr, Koh, C.A., 2007. Clathrate hydrates of natural gases. CRC press.

Song, G., Ning, Y., Guo, P., Li, Y., Wang, W., 2021. Investigation on hydrate growth at the oil–water interface: in the presence of wax and surfactant. Langmuir 37 (22), 6838–6845.

Song, G., Ning, Y., Li, Y., Wang, W., 2020. Investigation on hydrate growth at the oil–water interface: in the presence of wax and kinetic hydrate inhibitor. Langmuir 36 (48), 14881–14891.

Song, X., Wang, L., Yu, C., Chen, J., Ma, L., 2023. An experimental study on the interaction between hydrate formation and wax precipitation in waxy oil-in-water emulsions. Energy Eng. 120 (8), 1837–1852.

Sousa, A.M., Ribeiro, T.P., Pereira, M.J., Matos, H.A., 2023. How do methane, carbon dioxide or fatty acids affect waxy crude oils? Energies 16 (1), 406.

Theyab, M.A., 2018. Fluid flow assurance issues: literature review. SciFed Journal of Petroleum 2 (1), 1–11.

Tong, S., Wang, Z., Xie, K., Liu, J., Zhang, J., Fu, W., Sun, B., 2020. Experimental Study on the Methane Hydrate Formation in Water-in-oil Emulsions with Dissolved Wax. In: Abu Dhabi International Petroleum Exhibition & Conference. OnePetro.

Uchida, T., Hirano, T., Ebinuma, T., Narita, H., Gohara, K., Mae, S., Matsumoto, R., 1999. Raman spectroscopic determination of hydration number of methane hydrates. AlChE J. 45 (12), 2641–2645.

Vieira, L., Buchuid, M., Lucas, E., 2008. The influence of pressure and dissolved gases in petroleum on the efficiency of wax deposition inhibitors. Chemistry and Chemical Technology 02 (03), 211–215.

Vuolo, J.H., 1996. Fundamentos da teoria de erros. Editora Blucher.

Wang, W., Huang, Q., Zheng, H., Wang, Q., Zhang, D., Cheng, X., Li, R., 2020. Effect of wax on hydrate formation in water-in-oil emulsions. J. Dispers. Sci. Technol. 41 (12), 1821–1830.

Xiao, Y.-Y., Zhou, S.-D., Li, X.-Y., Wang, J.-J., Wu, Z.-M., Liu, Y., Lv, X.-F., 2023. Kinetic properties of CO2 hydrate formation in the wax-containing system at different concentrations. Energy & Fuels 37 (4), 2972–2982.

Zhang, D., Huang, Q., Zheng, H., Wang, W., Cheng, X., Li, R., Li, W., 2019. Effect of wax crystals on nucleation during gas hydrate formation. Energy & Fuels 33 (6), 5081–5090.

Zhou, S., Guo, Y., Lian, M., Liu, Y., Du, H., Lv, X., 2022. Study on the adhesion force between wax crystal particles and hydrate particles. ACS Omega 7 (6), 5283–5291.